AIAA JOURNAL
Vol. 43, No. 3, March 2005

Vortex Buffeting of Aircraft Tail: Interpretation via Proper Orthogonal Decomposition

Y. Kim* and D. Rockwell†
Lehigh University, Bethlehem, Pennsylvania 18015
and
A. Liakopoulos‡
University of Thessaly, 383 34 Volos, Greece

The proper-orthogonal-decomposition method is applied to particle-image-velocimetry (PIV) data to extract the most energetic flow structures of vortex-tail interaction. The reconstructed flowfields, in conjunction with patterns of vorticity and streamline topology, are compared with the original PIV data on a crossflow plane. The reconstructed flowfields using 5 and 10 eigenfunctions can predict the largest-scale features of the original flowfield. However, the smaller-scale flow structures, which are evident in the original PIV image, are lost. In other words, the flow features of smaller scale can be filtered out by employing the first few eigenmodes. By employing 40 eigenmodes, the reconstructed flowfield can reproduce most of the smaller-scale flow structures of the original flowfield. In terms of the kinetic energy of the fluctuations, about 80% of the total flow energy can be accounted for using 40 eigenmodes.

I. Introduction

THE interaction of a broken-down vortex with various types of physical configurations is generally recognized as a major source of the unsteady loading. Of particular interest for buffet loading of an aerodynamic surface is characterization of the frequency and amplitude of velocity and pressure fluctuations. Gursul and Xie[1] provided representations of the dimensionless frequency of vortex breakdown on delta wings. Detailed consideration of the power spectra of velocity fluctuations within the region of vortex breakdown has been assessed by Garg and Liebovich[2] and Gursul and Yang.[3] Moreover, Gursul and Yang[3] investigated the local pressure fluctuations at specified locations on a delta wing. The classification of pressure fluctuations in terms of dimensionless frequencies, which represent various features of the unsteady flow including vortex breakdown, was provided by Menke et al.[4] The helical mode of instability of vortex breakdown was viewed to play an important role in determining the unsteady surface loading. The unsteady features of this mode were described by Garg and Leibovich[2] and Gursul.[5] Reviews and assessments of the flow phenomena of the vortex breakdown include those of Sarpkaya,[6–8] Escudier,[9] Brown and Lopez,[10] and Delery.[11]

As reviewed by Rockwell,[12] a number of investigations have assessed the unsteady loading of an aircraft tail as a result of incident unsteadiness, typically arising from vortex breakdown. Representative investigations include those of Triplett,[13] Brown et al.,[14] and Komerath et al.,[15,16] Lee et al.[17] observed the vortical flow above an F/A-18 aircraft. In addition, results for a model F/A-18 with forebody and leading-edge extension configurations in water tunnel were found to be in accord with the wind tunnel and flight tests.[18] It is expected, however, that the detailed structure of the vortical flowfield after burst, or vortex breakdown, will generally be a function of both Reynolds number and Mach number. As a consequence, certain details of the flow structure characterized herein can be altered as one approaches values of parameters characteristic of full scale. The eventual objectives of any of the foregoing types of investigation are to gain an insight into the physical phenomena of the unsteady flowfield, in relation to the vortex breakdown and the corresponding loading induced at the aerodynamic surfaces. Numerical investigations of the unsteady loading on tail/fin include those of Kandil et al.,[19] Gordnier and Visbal,[20] and Kandil and Sheta.[21] Recent development of quantitative imaging techniques has provided instantaneous global patterns of the flow to allow rational interpretations of the unsteady loading caused by the vortex-plate and the vortex-tail configurations.[22] These approaches, which are based on a laser-scanning version of high-image-density particle image velocimetry (PIV), are addressed by Adrian,[23] Rockwell et al.,[24] and Westerweel.[25] More recently, Rockwell[26] assessed case studies of vortex-dominated flows using the technique of PIV.

II. Experimental System and Techniques

Experiments were conducted in a large-scale free-surface water channel having a cross section 927 mm wide, 610 mm high, and approximately 5000 mm long. It is located in the Fluid Mechanics Laboratory of Lehigh University. This recirculating water channel was constructed of optically transparent Plexiglas® with water reservoirs at the inlet and outlet ends. In this study, the flow velocity was maintained at 152 mm/s at a water depth of 559 mm. The corresponding Reynolds number based on the chord length of the delta wing was $Re_c = 5.2 \times 10^4$.

The plan and side views of the delta-wing-tail system are shown in Fig. 1. The laser sheet orientation is indicated. The tail is aligned with, or parallel to, the axis of the leading-edge vortex. The sweep angle of the wing is $\Lambda = 75$ deg, and the effective sweep angle of the leading-edge vortex is $\lambda_L = 79$ deg. The chord length of the wing is $C = 342$ mm. Moreover, the distance between the trailing edge of the wing and the leading edge of tail is $L_T = 5$ mm or $0.0146C$, and the angle of attack of the delta wing is $\alpha = 21$ deg for the experiment. The distance between the leading edge of the tail, at the root of the tail/delta-wing junction, and the plane of the laser sheet is indicated by $X_L = 0.965C_T$, where C_T (=105 mm) denotes the root chord length of the tail. Figure 2 shows the dimensions of the rigid tail. The tail had a root chord length of $C_T = 105$ mm, and the ratio of its thickness-to-chord ratio was $t_T/C_T = 0.12$. The span of the swept leading-edge of the tail was $S_T = 136$ mm. The length of the support

Received 10 April 2004; revision received 30 September 2004; accepted for publication 30 September 2004.

*Research Associate, Department of Mechanical Engineering and Mechanics, 367 Packard Laboratory, 19 Memorial Drive West.

†Paul B. Reinhold Professor, Department of Mechanical Engineering and Mechanics, 367 Packard Laboratory, 19 Memorial Drive West. Member AIAA.

‡Professor and Chairman, Department of Civil Engineering, Pedion Areos.

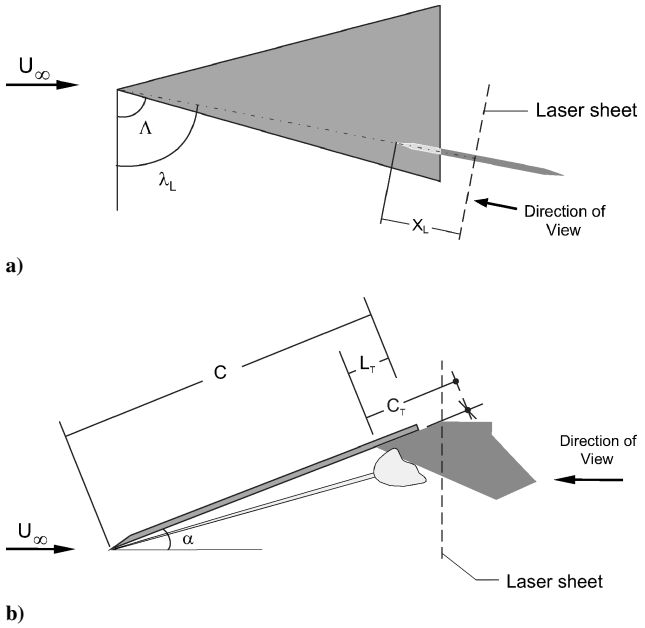

Fig. 1 Schematic of a) plan and b) side views of delta-wing-tail arrangement.

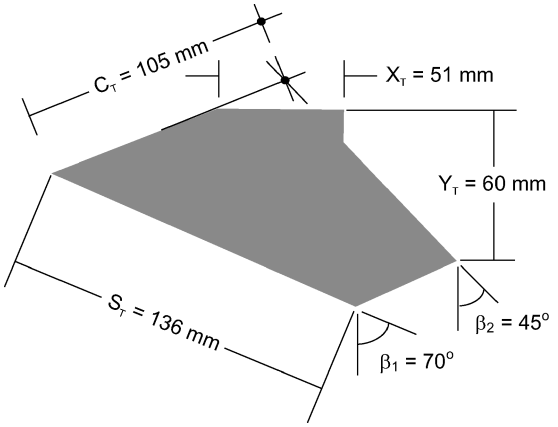

Fig. 2 Schematic of rigid tail.

strut of the tail was $X_T = 51$ mm, and the distance from the trailing edge of the tail tip to the support strut was $Y_T = 60$ mm, as indicated in Fig. 2. The angles of inclination of leading and trailing edges of the tail were $\beta_1 = 70$ deg and $\beta_2 = 45$ deg. In addition, both the leading and tip edges of the tail were beveled at an angle of 30 deg.

The delta-wing geometry is shown in Fig. 3. It was of Plexiglas® and had a leading-edge sweep angle $\Lambda = 75$ deg, a chord $C = 342$ mm, and a thickness-to-chord ratio $t_w/C = 0.028$. The leading edges were beveled at an angle of 30 deg on each side of the wing. Therefore, the sharp leading edge of the wing provided a stable separation point.

In this study, high-image-density digital particle image velocimetry (DPIV) was employed by illuminating the flowfield to obtain instantaneous images of small scattering particles. Comprehensive reviews of application of the PIV technique are given by Adrian,[23] Rockwell et al.,[24] and Westerweel.[25] For DPIV, the motion of neutrally buoyant particles in water is analyzed using the image cross-correlation technique to determine the two-dimensional velocity field. The scattering particles are metallic-coated glass spheres with a mean diameter of 14 μ. They are manufactured by Potters Industries, Inc. These particles were illuminated by a laser sheet approximately 1 mm thick. It was generated from a Nd:Yag (90 mJ) double-pulsed laser.

A two-frame cross-correlation technique was employed to determine two-dimensional velocity data for a given interrogation

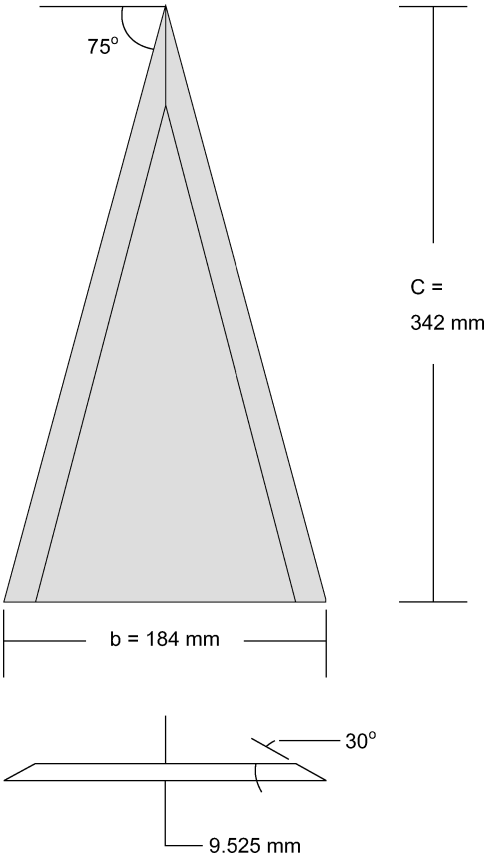

Fig. 3 Schematic of delta wing.

window with a 50% overlap to satisfy the Nyquist criterion. The frame-to-frame cross-correlation technique allows the velocity to be measured without any directional ambiguity. The framing rate of 67 ms, or 15 Hz, between frame pairs was applied throughout the experiment. The magnification factor (MF) of the lens was calculated as the ratio of a length in pixels as it appears on the recorded image to the actual physical length in millimeters. An image was taken to determine the scale by locating a millimeter scale parallel to the laser sheet. This approach led to the value of the MF. The value of MF was 1:7.54 in this study, which gave an effective grid size of 2.12 mm in the plane of the laser sheet. The grid size in a given image was 61 pixels in the x direction and 62 pixels in the y direction, which yields a total of 3782 vectors in the field of view.

III. Proper Orthogonal Decomposition

A. Previous Related Investigations

The proper-orthogonal-decomposition (POD) technique was first considered in the field of fluid mechanics by Lumley,[27] in order to identify the dynamical coherent flow structures in turbulent flows. Meteorologists have been referring to the decomposition as the method of orthogonal empirical eigenfunction. Karhunen–Loeve expansion is a term also used widely in the literature. Berkooz et al.[28] have reviewed the important issues in applying POD to turbulent flows. Various unsteady flow configurations have been investigated via POD. They include a turbulent boundary layer,[29,30] a mixing layer,[31–33] flow past an open cavity, grooved channels and circular cylinders,[34–36] flow in an enclosure and a vertical channel,[37,38] a turbulent jet,[39–42] and flow past a delta wing.[43]

The POD technique extracts the most energetic eigenmodes by retaining only a small number of modes that capture most of the fluctuation energy. The PIV technique of the present study allows, in effect, acquisition of sequential velocity data at a large number of spatial points simultaneously, and so it provides an attractive basis for POD. The snapshot version of POD, which was developed by Sirovich,[44] is particularly relevant to the present investigation. In this technique, empirical eigenfunctions are extracted

from spatiotemporal data sets, obtained from either experiments or numerical computations. In the present study, this snapshot version of POD is applied to the original PIV images of the flowfield. The POD simulation carried out herein is focused on vortex breakdown-tail interaction at a relatively low value of Reynolds number. The required number of modes to characterize a substantial portion of the energy of the flowfield might be different for a value of Reynolds number approaching full scale.

Previous investigations show that the flowfield reconstructed via POD can accurately describe the original flow structure even with few empirical eigenfunctions in some cases. Furthermore, this procedure can be used also as a tool for the elimination of some of the extraneous small-scale features of the flow.

Direct numerical simulation of a turbulent flow requires a formidable amount of computing time and memory. Therefore, low-dimensional models are desirable. Deane et al.[34] described low-dimensional models for flows past a grooved channel and circular cylinders. By employing a Galerkin method, a governing partial differential equation can be reduced to a system of first-order ordinary differential equations.[38,45]

The topic of the present investigation is a highly complex, separated turbulent flow along the surface of an aircraft tail. Although this flow does show, to a degree, deterministic behavior as a result of the onset of vortex breakdown, the downstream region of the flow structure is certainly not periodic, as it rapidly degenerates to a quasi-turbulent flow with a low degree of coherence. It is therefore appropriate to employ a POD technique in order to make simulation of this flow more efficient and to serve as an eventual basis for flow control.

B. Present Method

Assuming that M snapshots of the instantaneous velocity field are available from PIV or numerical flow simulation, the POD methodology proceeds as follows. In the first step, the time-dependent velocity field data are decomposed into time-averaged and fluctuation components, that is,

$$\boldsymbol{V}(x, y, t) = \bar{\boldsymbol{V}}(x, y) + \boldsymbol{V}'(x, y, t) \tag{1}$$

where $\boldsymbol{V}'$ and $\bar{\boldsymbol{V}}$ denote the fluctuation and time-averaged velocities, and boldface symbols denote vector quantities. The value of $\bar{\boldsymbol{V}}$ is obtained by calculating the average of M snapshots of the velocity field, that is,

$$\bar{\boldsymbol{V}}(x, y) = \frac{1}{M}\sum_{i=1}^{M} \boldsymbol{V}(x, y, t_i) \tag{2}$$

Evidently, the fluctuating component of the velocity is readily available from Eqs. (1) and (2), that is,

$$\boldsymbol{V}'(x, y, t) = \boldsymbol{V}(x, y, t) - \bar{\boldsymbol{V}}(x, y) \tag{3}$$

In the next step, the empirical eigenfunctions ($\phi_k, k = 1, 2, \ldots, M$) are constructed by an appropriate superposition of the fluctuation components of the instantaneous data, as suggested by Sirovich,[44] that is,

$$\phi_\kappa(x, y) = \sum_{i=1}^{M} A_{\mathrm{ki}} \boldsymbol{V}_i'(x, y, t_i) \tag{4}$$

where $\boldsymbol{V}_i'$ denotes the ith fluctuation velocity field, that is, the fluctuation velocity at $t = t_i$, and A_k represents the kth eigenvector of the algebraic eigenvalue problem

$$CA = \lambda A \tag{5}$$

In Eq. (5), C is an $M \times M$ square symmetric real matrix whose elements are given by

$$C_{\mathrm{mn}} = \frac{1}{M}\int_\Omega F_{\mathrm{mn}}(x, y, t)\, \mathrm{d}\Omega \tag{6}$$

Here,

$$F_{\mathrm{mn}} = \boldsymbol{V}_m'(x, y, t_m) \cdot \boldsymbol{V}_n'(x, y, t_n) \tag{7}$$

and Ω indicates the processing domain. In Eq. (7), the dot denotes the inner product between $\boldsymbol{V}_m'$ and $\boldsymbol{V}_n'$. Having constructed matrix C, the eigenvalue problem, Eq. (5), is solved, and the eigenvalues ($\lambda_1, \lambda_2, \ldots, \lambda_M$) of C and its corresponding eigenvectors ($A_1, A_2, \ldots, A_M$) can be computed. Note that all eigenvalues are real, nonnegative, and can be arranged in descending order such that $\lambda_1 \geq \lambda_2 \geq \ldots \geq \lambda_M$. Each eigenvalue represents the flow kinetic energy contributed by the corresponding eigenfunction. Note also that

$$\sum_{i=1}^{M} \lambda_i = 1$$

that is, the sum of all eigenvalues reflects the total fluctuation flow energy. It turns out that the fluctuation velocity field can be approximated by a truncated series expansion of the form

$$\boldsymbol{V}'(x, y, t) = \sum_{k=1}^{N} a_k(t)\phi_k(x, y) \tag{8}$$

where the value of N is usually selected to be much less than the total number of snapshots M and a_k, which is time dependent, can be determined by using the orthonormality property of eigenfunctions, that is,

$$a_k(t) = \int_\Omega \boldsymbol{V}'(x, y, t) \cdot \phi_\kappa(x, y)\, \mathrm{d}\Omega \tag{9}$$

Finally, we note that the instantaneous flowfield can be reconstructed according to

$$\boldsymbol{V}(x, y, t) = \bar{\boldsymbol{V}}(x, y) + \sum_{k=1}^{N} a_k(t)\phi_k(x, y) \tag{10}$$

IV. Onset of the Vortex Breakdown

Figure 4 represents the location of the onset of the vortex breakdown via dye visualization and patterns of averaged vorticity $\langle\omega\rangle$.

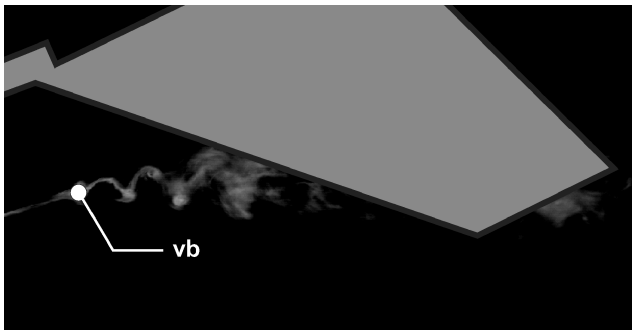

a)

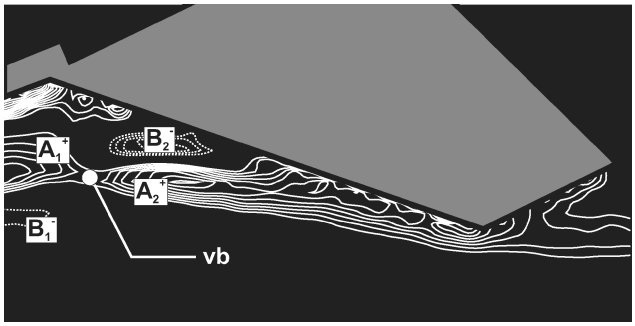

b)

Fig. 4 Location of the onset of vortex breakdown (vb): a) dye visualization and b) patterns of averaged vorticity.

Obviously a spiral type of vortex breakdown can be observed in the dye image (Fig. 4a). Furthermore, the location of sign changes in layers of averaged vorticity (Fig. 4b), as indicated by A_1^+, A_2^+, B_1^-, and B_2^-, clearly identifies the onset of vortex breakdown in the dye visualization (Fig. 4a).

V. Assessment of Flow Structures via POD

In the present study, $M = 137$ snapshots of the velocity data from PIV were employed in the POD analysis.

A. Patterns of Empirical Eigenfunctions

Figure 5 exhibits the fluctuating component of velocity and patterns of vorticity of the selected empirical eigenfunctions; $\phi_1, \phi_2, \phi_5, \phi_{10}, \phi_{20}$, and ϕ_{40}. These eigenfunctions were obtained from Eq. (4) in Sec. III. The first two eigenfunctions represent the large-scale features of the flow and reflect the most energetic modes. On the other hand, the smaller-scale flow structures can only be captured by computing the high-order eigenfunctions, which is also clearly evident in the plots of vorticity. In the plots of vorticity contours, solid lines indicate positive vorticity, and dashed lines represent negative vorticity.

B. Patterns of Instantaneous Velocity and Vorticity

Figure 6 shows comparisons of the original instantaneous PIV flowfields and the reconstructed flowfields using 10, 20, and 40 eigenfunctions. It is clear that the reconstructed flowfield using 10 eigenfunctions can predict certain of the largest-scale features of the flow structure, even on the outboard (right) side of the tail. However, the smaller scales of the flow structure, evident in the instantaneous PIV image, are not observed in the reconstructed flowfield.

It is evident, however, that the flowfield reconstructed with 20 eigenfunctions shows smaller, more detailed features than the preceding case using a smaller number of eigenfunctions. The vortical flow structure on the inboard (left) side of the tail is generally predicted in this image.

Furthermore even smaller-scale flow features can be extracted with 40 eigenfunctions. Obviously, the reconstructed flowfield does not reproduce all of the characteristics of the original PIV flow structure. The overall form of the secondary (positive) vortex structure on the outboard (right) side of the tail starts to resemble the form shown in the original PIV image.

Figure 7 presents the flowfields reconstructed from 40 eigenfunctions at other instants of time, along with the corresponding original PIV data. It is obvious that the large-scale flow features of the original PIV flowfield can, in effect, be reconstructed by employing 40 eigenmodes. However, the small-scale flow structures are only marginally reproduced, as shown in the images.

C. Comparison of Patterns of Streamline Topology

Figure 8 presents the patterns of the streamlines of the reconstructed flowfield using 5, 10, 20, and 40 eigenmodes, respectively. The corresponding streamline pattern of the original PIV data is shown in Fig. 8e. In Fig. 8a, the reconstructed flowfield involves five eigenmodes. The streamline pattern on the inboard (left) side of the tail indicates extended inward spirals along the tail surface. Moreover, the streamline patterns on the outboard (right) side of the tail show large-scale swirling motion. However, the streamline patterns of the original PIV data (Fig. 8e) have a form quite different from the reconstructed flowfield. In the image of original PIV data (Fig. 8e), the streamlines on the inboard (left) side of the tail show

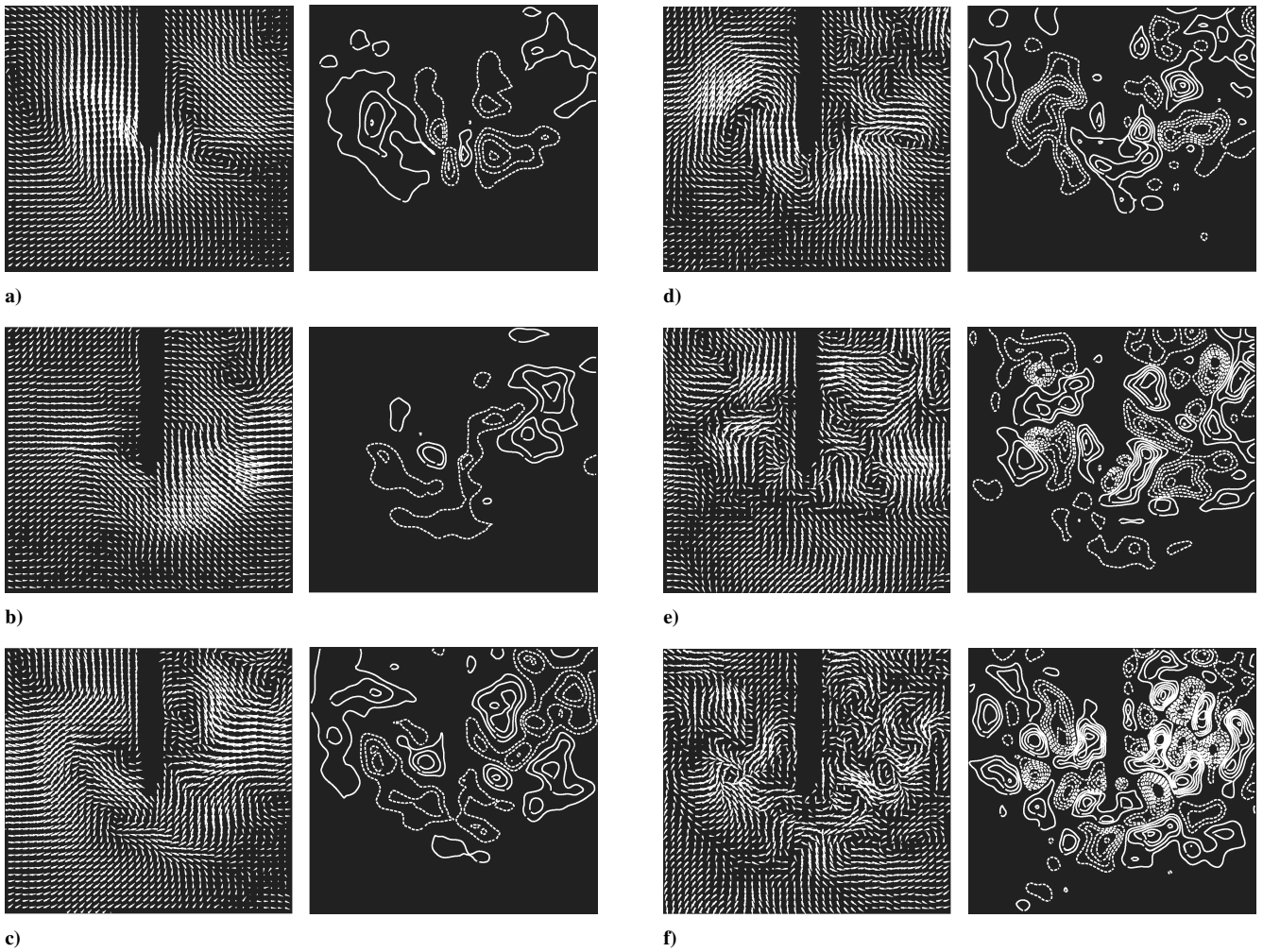

Fig. 5 Selected eigenfunctions for the fluctuating component of velocity and vorticity contours: a) ϕ_1, b) ϕ_2, c) ϕ_5, d) ϕ_{10}, e) ϕ_{20}, and f) ϕ_{40}.

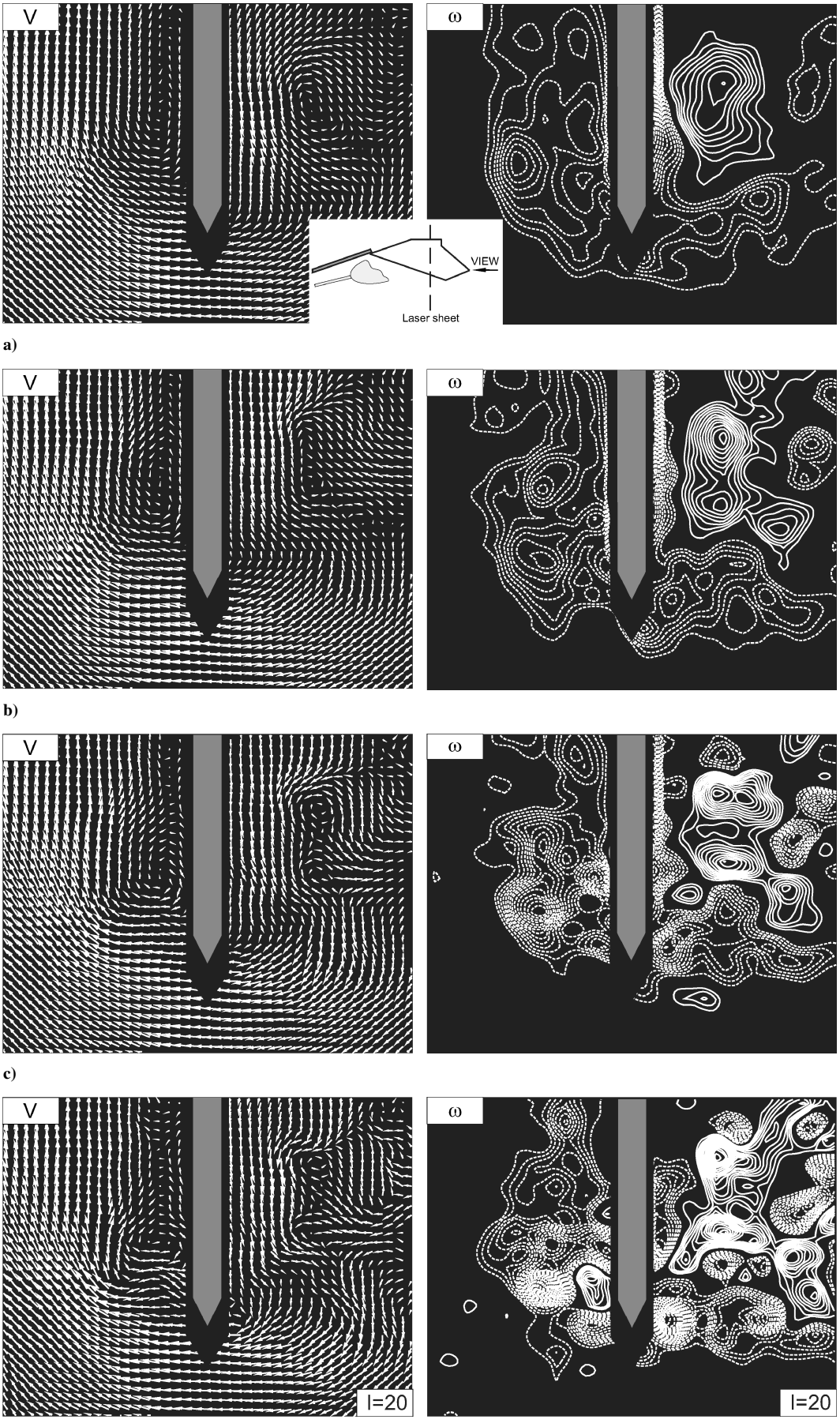

Fig. 6 Reconstructed velocity fields and patterns of vorticity using a) 10, b) 20, and c) 40 eigenmodes in association with d) original PIV data in a crossflow plane; minimum and incremental vorticity levels are as follows: $\omega_{min} = \pm 2 s^{-1}$, and $\Delta\omega = 1 s^{-1}$.

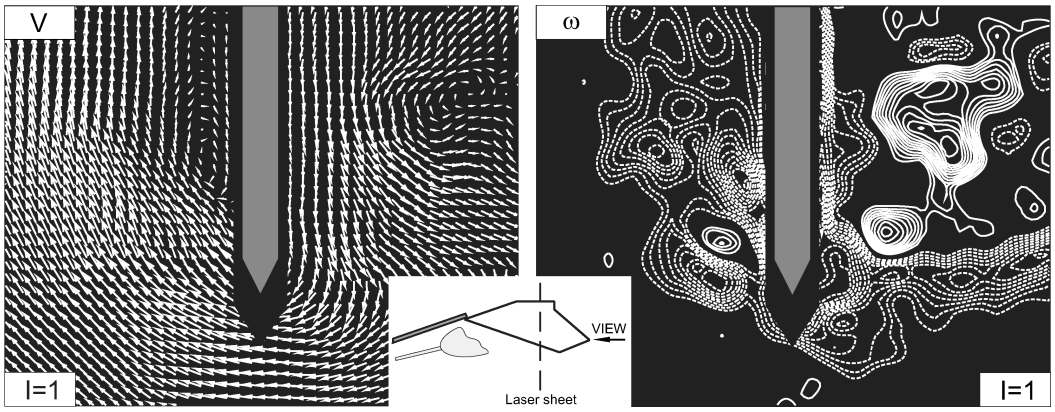

a)

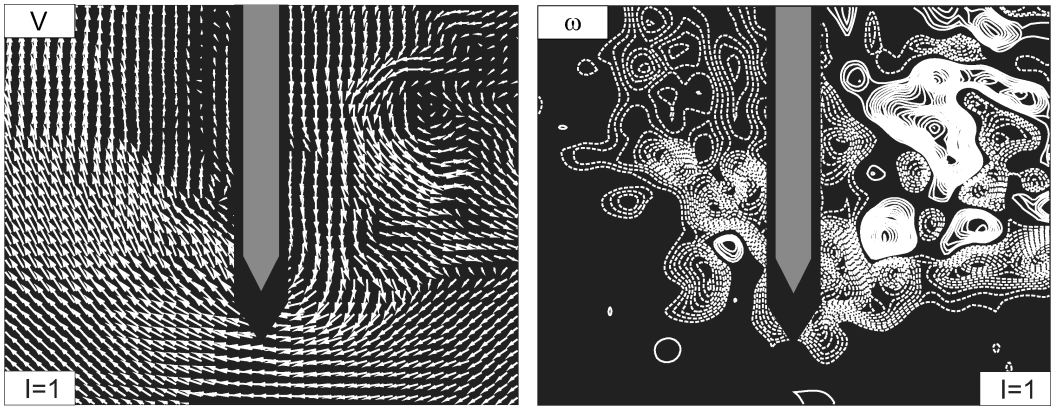

b)

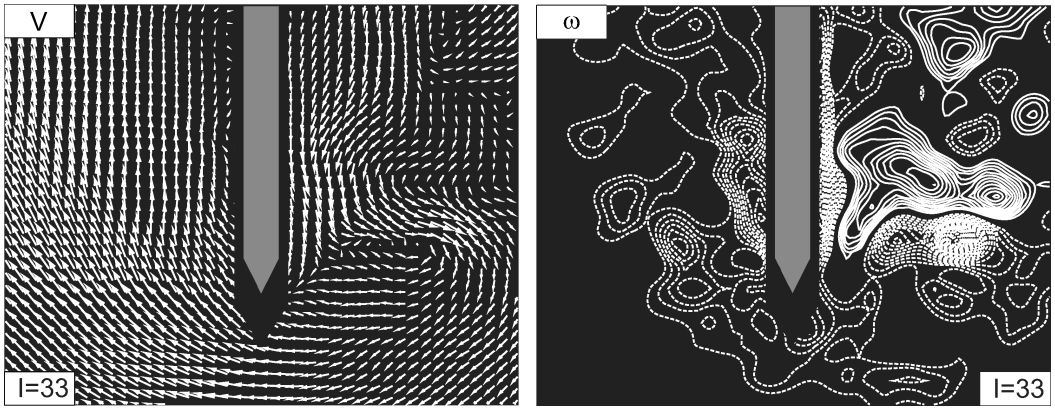

c)

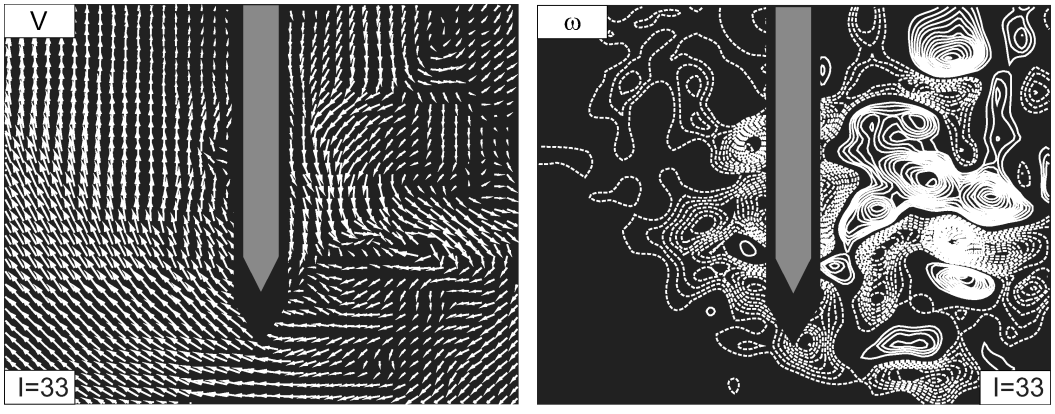

d)

Fig. 7 Reconstructed velocity fields and patterns of vorticity using a) 40 eigenmodes in association with b) original PIV data at the specific instant $I = 1$, and reconstructed velocity fields and patterns of vorticity using c) 40 eigenmodes in association with d) original PIV data at the specific instant $I = 33$ in a crossflow plane; minimum and incremental vorticity levels are as follows: $\omega_{min} = \pm 2s^{-1}$, and $\Delta\omega = 1s^{-1}$.

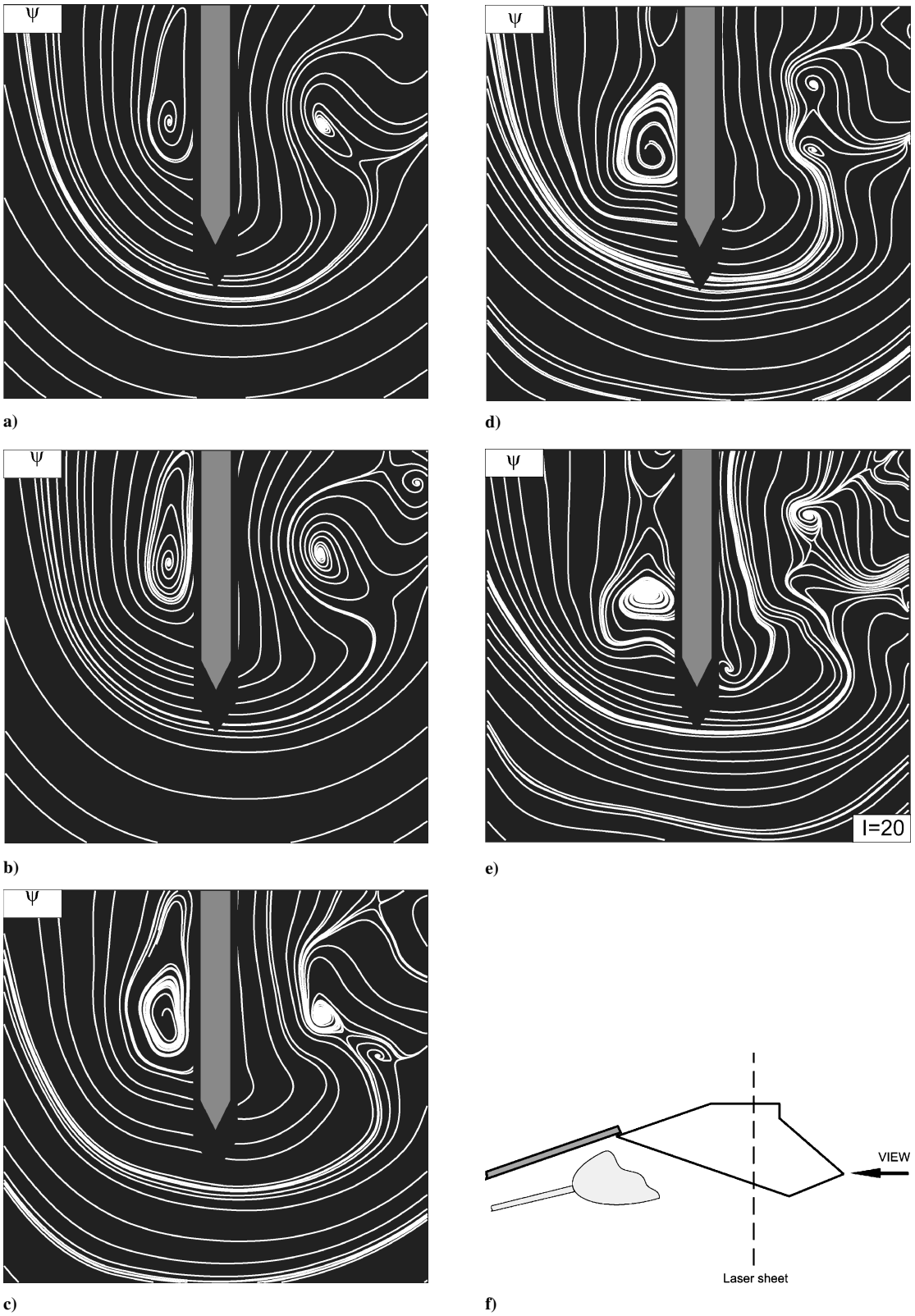

Fig. 8 Comparison of patterns of streamlines using a) 5, b) 10, c) 20, and d) 40 eigenmodes in association with e) original PIV data on f) laser sheet plane.

concentrated, inward spiraling patterns. On the outboard (right) side of the tail of the original PIV image (Fig. 8e), the original streamline patterns are also characterized by much more complicated topology than shown in the reconstructed flowfield. From this comparison between the reconstructed flowfield and the original PIV data, it is quite obvious that the reconstructed flowfield from five eigenmodes in Fig. 8a has insufficient information to represent accurately the original PIV flowfield (Fig. 8e).

The patterns of instantaneous streamlines of the reconstructed flowfield using 10 eigenmodes are shown in Fig. 8b. It is quite evident that the streamline patterns of the reconstructed flowfield in the image are somewhat similar to the patterns of the reconstructed flowfield from five eigenmodes, as shown in Fig. 8a. In other words, the reconstructed flowfield from 10 eigenmodes in Fig. 8b does not indicate a significant gain and is not capable of adequately representing the original PIV flowfield (Fig. 8e).

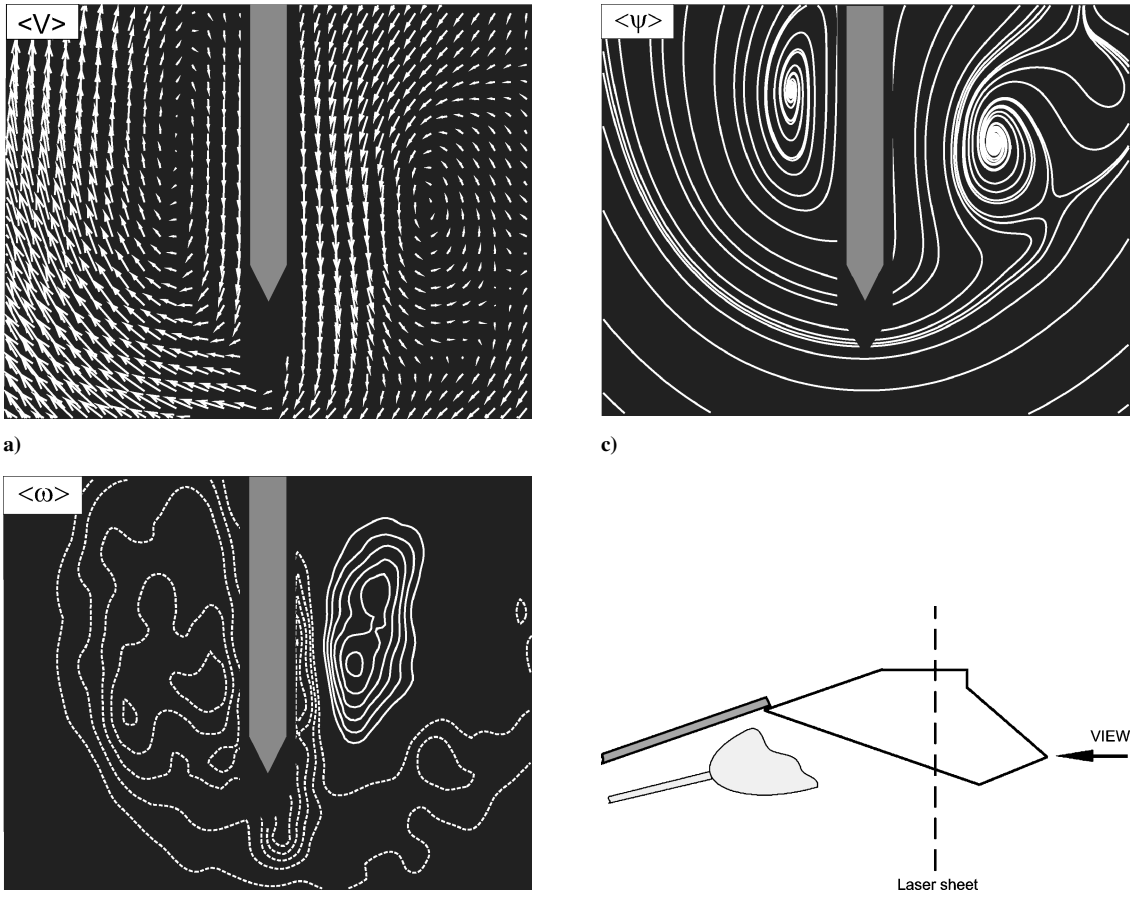

Fig. 9 Averaged patterns of a) velocity $\langle V \rangle$, b) vorticity $\langle \omega \rangle$, and c) streamline $\langle \psi \rangle$ on d) laser sheet plane; minimum and incremental values of parameters are as follows: $\langle \omega \rangle_{\min} = \pm 2 s^{-1}$, and $\Delta \langle \omega \rangle = 1 s^{-1}$.

In Fig. 8c, the patterns of instantaneous streamlines of the reconstructed flowfield using 20 eigenmodes yield a more detailed representation of the original PIV flowfield (Fig. 8e), relative to the flowfield obtained from the lower number of eigenmodes presented in Figs. 8a and 8b. Despite this more detailed reconstruction, the complex streamline patterns on the outboard (right) side of the tail in the original PIV (Fig. 8e) are still not adequately represented. Moreover, on the inboard (left) side of the tail, the streamline patterns are similar to those presented from 5 and 10 eigenmodes cases.

Figure 8d presents patterns of the instantaneous streamline patterns of the reconstructed flowfield using 40 eigenmodes, in relation to the original PIV data (Fig. 8e). Obviously, the streamline patterns of the reconstructed flowfield on the inboard (left) side of the tail clearly start to resemble the patterns of the original PIV data. In addition, the patterns show the complex features on the outboard (right) side of the tail, thereby representing reasonably well the topology of the original PIV flowfield.

D. Patterns of Averaged Velocity, Vorticity, and Streamline Topology

Figure 9 shows patterns of averaged velocity $\langle V \rangle$, vorticity $\langle \omega \rangle$, and streamline $\langle \psi \rangle$ topology based on the original PIV data. Inward spiral patterns are observable on the inboard (left) side of the tail, and the large-scale patterns of the well-organized swirling motion can be clearly found on the outboard (right) side of the tail.

E. Time-Dependent Coefficients, Normalized Eigenvalues, and Cumulative Flow Energy

Figure 10 shows selected time-dependent coefficients $a_k(t)$, which are computed according to Eq. (9) in Sec. III. The first seven most energetic modes are presented. The first temporal expansion coefficient $a_1(t)$ is randomly distributed throughout the sampling time of the PIV data. The second coefficient $a_2(t)$ and the third coefficient $a_3(t)$ display higher frequency features. Moreover, their amplitudes are smaller; they represent the small-scale structures of the second and third eigenfunctions, respectively. For the higher mode coefficients, a similar trend, at even higher frequency and smaller amplitude, can be clearly observed in the plot.

Table 1 POD analysis of flow patterns in a crossflow plane: normalized eigenvalues and cumulative flow energy contribution vs eigenmode number

Eigenmode number	Normalized eigenvalue	Cumulative flow energy, %
1	0.1382	13.82
2	0.0897	22.79
3	0.0644	29.23
4	0.0434	33.57
5	0.0366	37.23
6	0.0307	40.30
7	0.0294	43.24
8	0.0260	45.84
9	0.0231	48.15
10	0.0210	50.25
20	0.0112	64.83
40	0.0052	79.56

Table 1 shows normalized eigenvalues and cumulative flow fluctuation energy according to the eigenmode number. The first two eigenmodes contribute 22.79% of the total flow fluctuation energy, whereas the first six eigenmodes reproduce up to 40.30% of the total energy. The cumulative flow energy level can reach 50.25% of the total with 10 eigenmodes. In addition, with 40 eigenmodes the

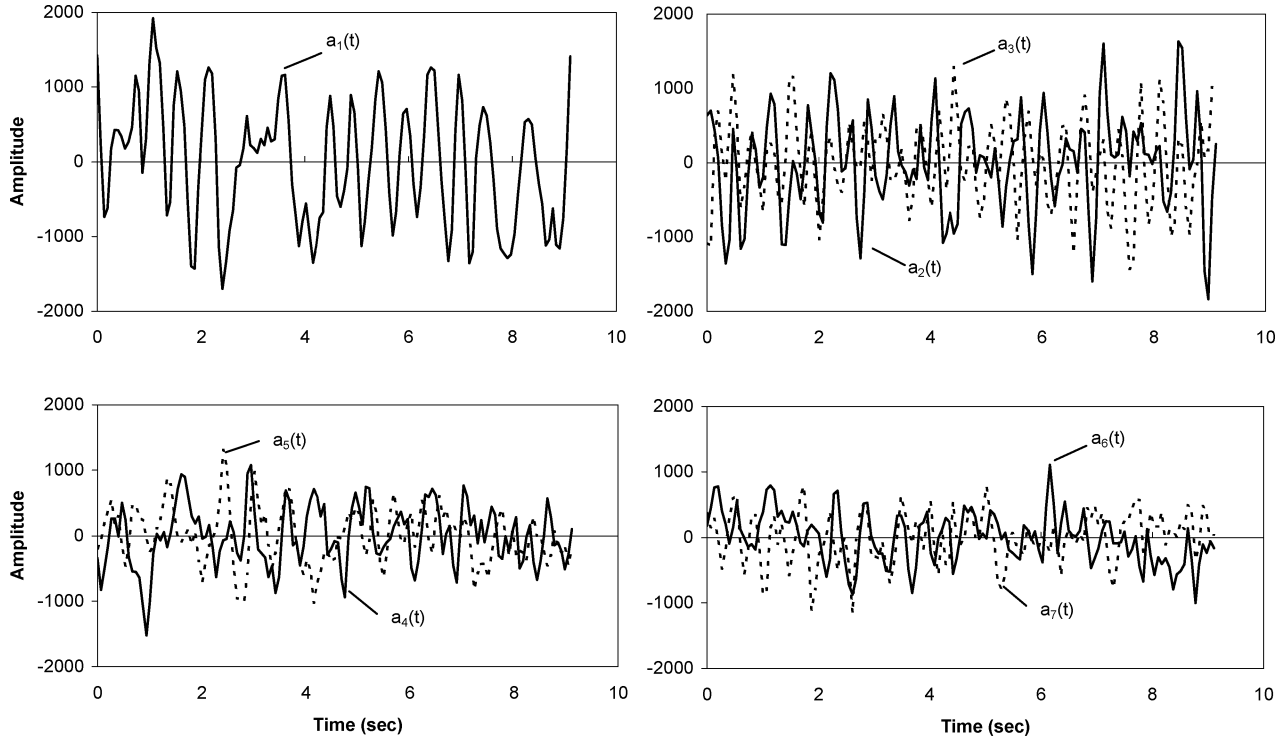

Fig. 10 Expansion coefficients for the seven most energetic modes.

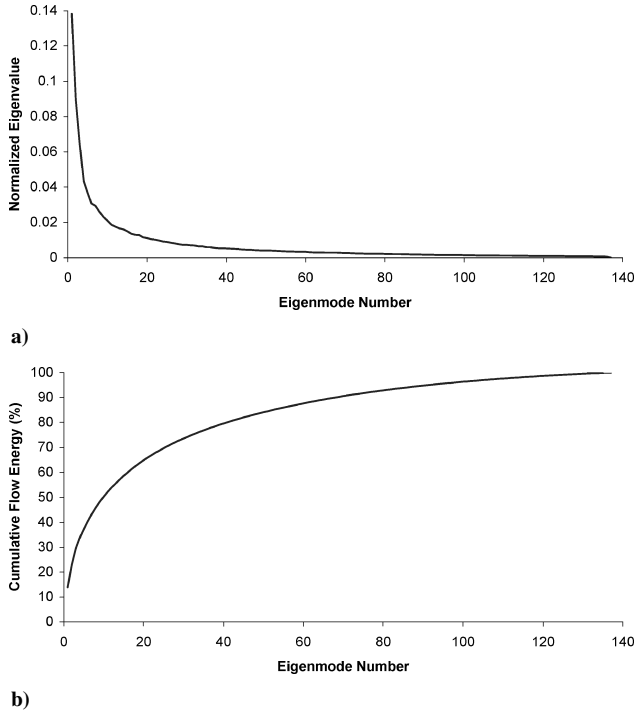

Fig. 11 Relation of eigenmode number to a) normalized eigenvalue and b) cumulative flow energy (%).

reconstructed flowfield, which contains 79.56% of flow energy, can predict the major features of the original PIV flowfield.

Figure 11a displays the distribution of normalized eigenvalues with respect to the 137 eigenmodes. It can be observed that the eigenvalues decrease very rapidly for the first 10 eigenmodes. However, the eigenvalues decrease gradually and converge to zero value beyond the first 40 eigenmodes. Figure 11b exhibits the cumulative flow energy according to the 137 eigenmodes. About 84% of flow energy can be captured by employing the first 50 eigenmodes.

VI. Conclusions

Flow structures associated with vortex-tail interaction, viewed on a crossflow plane, have been analyzed via proper orthogonal decomposition (POD). The POD method is applied to the instantaneous sequential data from particle-image-velocimetry (PIV) experiments to extract the most energetic phenomena of the flow.

Comparisons of patterns of instantaneous velocity and vorticity between the original instantaneous PIV data and the reconstructed flowfields using 5 and 10 empirical eigenfunctions show that the reconstructed flowfield can extract the largest-scale features of the flow, whereas the smaller scales of the flowfield are not reproduced in the reconstructed flowfield. This is rather expected by noticing (see Fig. 11b) that, based on the analysis, the reconstructed flowfields from 5 and 10 eigenmodes contribute, respectively, about 37 and 50% of the total flow energy.

Furthermore, even the smaller-scale flow features can be predicted with higher eigenmodes by employing 20 and 40 eigenfunctions. However, the reconstructed flowfield does not predict all of the flow features of the original PIV data. About 80% of flow energy, in fact, can be accounted for by employing the first 40 eigenmodes. In addition, the amplitudes of the higher-mode, time-dependent coefficients are smaller, which reflect the smaller-scale flow features.

An overall comparison between the streamline patterns of the reconstructed flowfield using different eigenmodes and the corresponding original PIV data is also presented. It is quite interesting to observe that the streamline patterns obtained from 10 eigenmodes are of somewhat identical form to the patterns from five eigenmodes: extended inward spiral patterns form along the inboard (left) side of the tail, whereas the large-scale features of swirling motion occur on the outboard (right) side of the tail. In the image of the reconstructed field from 20 eigenmodes, the streamline topology on the inboard (left) side of the tail shows similarity to the patterns corresponding to 5 and 10 eigenmodes. However, on the outboard (right) side of the tail, the complex, small-scale features, obvious in the instantaneous original PIV image, can be observed. Moreover, the streamline patterns from 40 eigenmodes can yield more detailed, smaller-scale flow features of the original PIV flowfield: extended inward spirals begin to appear along the inboard (left) side of the tail, and more complicated streamline topology becomes apparent on the outboard (right) side of the tail.

In summary, the reconstructed flow structures via POD analysis using the first few eigenmodes can extract successfully the dominant spatial features and the most energetic flow structures of the original PIV data, whereas more complicated spatial flow features and short-time phenomena can be reproduced by the higher eigenmodes.

Acknowledgments

The authors gratefully acknowledge support of this research under U.S. Air Force Office of Scientific Research Grants F49620-00-1-0009 and F49620-02-1-0061, monitored by Steven Walker and John Schmisseur. In addition, supplemental funding for instrumentation was provided by U.S. Office of Naval Research Grants N00014-99-1-0581 and N0014-01-1-0606.

References

[1]Gursul, I., and Xie, W., "Physics of Buffeting Flows over Delta Wings," AIAA Paper 98-0688, Jan. 1998.

[2]Garg, A. K., and Leibovich, S., "Spectral Characteristics of Vortex Breakdown Flowfields," *Physics of Fluids*, Vol. 22, No. 11, 1979, pp. 2053–2064.

[3]Gursul, I., and Yang, H., "On Fluctuations of Vortex Breakdown Location," *Physics of Fluids*, Vol. 7, No. 1, 1995, pp. 229–231.

[4]Menke, M., Yang, H., and Gursul, I., "Further Experiments on Fluctuations of Vortex Breakdown Location," AIAA Paper 96-0205, Jan. 1996.

[5]Gursul, I., "Unsteady Flow Phenomena over Delta Wings at High Angle-of-Attack," *AIAA Journal*, Vol. 32, No. 2, 1994, pp. 225–231.

[6]Sarpkaya, T., "On Stationary and Traveling Vortex Breakdowns," *Journal of Fluid Mechanics*, Vol. 45, No. 3, 1971, pp. 545–559.

[7]Sarpkaya, T., "Vortex Breakdown in Swirling Conical Flows," *AIAA Journal*, Vol. 9, No. 9, 1971, pp. 1792–1799.

[8]Sarpkaya, T., "Effect of the Average Pressure Gradient on Vortex Breakdown," *AIAA Journal*, Vol. 12, No. 5, 1974, pp. 602–607.

[9]Escudier, M., "Vortex Breakdown: Observations and Explanations," *Progress in Aerospace Sciences*, Vol. 25, No. 2, 1988, pp. 189–229.

[10]Brown, G. L., and Lopez, J. M., "Axisymmetric Vortex Breakdown. Part 2. Physical Mechanisms," *Journal of Fluid Mechanics*, Vol. 221, 1990, pp. 553–576.

[11]Delery, J. M., "Aspects of Vortex Breakdown," *Progress in Aerospace Sciences*, Vol. 30, No. 1, 1994, pp. 1–59.

[12]Rockwell, D., "Vortex-Body Interactions," *Annual Review of Fluid Mechanics*, Vol. 30, 1998, pp. 199–229.

[13]Triplett, W. E., "Pressure Measurements on Twin Vertical Tails in Buffeting Flow," *Journal of Aircraft*, Vol. 20, No. 11, 1983, pp. 920–925.

[14]Brown, D., Lee, B. H. K., and Tang, F. C., "Some Characteristics and Effects of the F/A-18 Lex Vortices," Vortex Flow Aerodynamics, AGARD CP 494, 1990, pp. 30-1–30-20.

[15]Komerath, N. M., Liou, S. G., Schwartz, R. J., and Kim, J. M., "Flow over a Twin-Tailed Aircraft at Angle of Attack, Part I: Spatial Characteristics," *Journal of Aircraft*, Vol. 29, No. 3, 1992, pp. 413–420.

[16]Komerath, N. M., Liou, S. G., Schwartz, R. J., and Kim, J. M., "Flow over a Twin-Tailed Aircraft at Angle of Attack, Part II: Temporal Characteristics," *Journal of Aircraft*, Vol. 29, No. 4, 1992, pp. 553–558.

[17]Lee, J. W., Cavone, A. A., and Suzuki, K. E., "Doppler Global Velocimetry Measurements of the Vortical Flow Above an F/A-18," AIAA Paper 93-0414, Jan. 1993.

[18]Lee, B. H. K., "Vertical Tail Buffeting of Fighter Aircraft," *Progress in Aerospace Sciences*, Vol. 36, No. 3–4, 2000, pp. 193–279.

[19]Kandil, O. A., Sheta, E. F., and Massey, S. J., "Buffet Responses of a Vertical Tail in Vortex Breakdown Flows," AIAA Paper 95-3464, 1995.

[20]Gordnier, R. E., and Visbal, M. R., "Numerical Simulation of the Impingement of a Streamwise Vortex on a Plate," AIAA Paper 97-1781, June–July 1997.

[21]Kandil, O. A., and Sheta, E. F., "Coupled and Uncoupled Bending-Torsion Responses of Twin-Tail Buffet," *Journal of Fluids and Structures*, Vol. 12, No. 6, 1998, pp. 677–701.

[22]Kim, Y., Ozgoren, M., and Rockwell, D., "Vortex Breakdown-Tail Interaction," *AIAA Journal*, Vol. 41, No. 3, 2003, pp. 544–549.

[23]Adrian, R. J., "Particle–Imaging Techniques for Experimental Fluid Mechanics," *Annual Review of Fluid Mechanics*, Vol. 23, 1991, pp. 261–304.

[24]Rockwell, D., Magness, C., Towfighi, J., Akin, O., and Corcoran, T., "High Image-Density Particle Image Velocimetry Using Laser Scanning Techniques," *Experiments in Fluids*, Vol. 14, No. 3, 1993, pp. 181–192.

[25]Westerweel, J., "Fundamentals of Digital Particle Image Velocimetry," *Measurement Science Technology*, Vol. 8, No. 12, 1997, pp. 1379–1392.

[26]Rockwell, D., "Imaging of Unsteady Separated Flows: Global Interpretation with Particle Image Velocimetry," *Experiments in Fluids* [Suppl.], 2000, pp. S255–S273.

[27]Lumley, J. L., *Atmospheric Turbulence and Radio Wave Propagation*, edited by A. M. Yaglom and V. I. Tatarski, Navko, Moscow, 1967, pp. 160–178.

[28]Berkooz, G., Holmes, P., and Lumley, J. L., "The Proper Orthogonal Decomposition in the Analysis of Turbulent Flows," *Annual Review of Fluid Mechanics*, Vol. 25, 1993, pp. 539–575.

[29]Aubry, N., Holmes, P., Lumley, J. L., and Stone, E., "The Dynamics of Coherent Structures in the Wall Region of a Turbulent Boundary Layer," *Journal of Fluid Mechanics*, Vol. 192, 1988, pp. 115–173.

[30]Rempfer, D., and Fasel, H. F., "Evolution of Three-Dimensional Coherent Structures in a Flat-Plate Boundary Layer," *Journal of Fluid Mechanics*, Vol. 260, 1994, pp. 351–375.

[31]Glezer, A., Kadioglu, Z., and Pearlstein, A. J., "Development of an Extended Proper Orthogonal Decomposition and Its Application to a Time Periodically Forced Plane Mixing Layer," *Physics of Fluids A*, Vol. 1, No. 8, 1989, pp. 1363–1373.

[32]Delville, J., Ukeiley, L., Cordier, L., Bonnet, J. P., and Glauser, M., "Examination of Large-Scale Structures in a Turbulent Plane Mixing Layer. Part 1. Proper Orthogonal Decomposition," *Journal of Fluid Mechanics*, Vol. 391, 1999, pp. 91–122.

[33]Citriniti, J. H., and George, W. K., "Reconstruction of the Global Velocity Field in the Axisymmetric Mixing Layer Utilizing the Proper Orthogonal Decomposition," *Journal of Fluid Mechanics*, Vol. 418, 2000, pp. 137–166.

[34]Deane, A. E., Kevrekidis, I. G., Karniadakis, G. E., and Orszag, S. A., "Low Dimensional Models for Complex Geometry Flows: Application to Grooved Channels and Circular Cylinders," *Physics of Fluids A*, Vol. 3, No. 10, 1991, pp. 2337–2354.

[35]Sahan, R. A., Liakopoulos, A., and Gunes, H., "Reduced Dynamical Models of Nonisothermal Transitional Grooved-Channel Flow," *Physics of Fluids*, Vol. 9, No. 3, 1997, pp. 551–565.

[36]Rona, A., and Brooksbank, E. J., "POD Analysis of Cavity Flow Instability," AIAA Paper 2003-0178, Jan. 2003.

[37]Kim, Y., "Construction of Low-Dimensional Models of Thermo-Fluid Systems: A Fully Spectral Technique," M.S. Thesis, Dept. of Mechanical Engineering and Mechanics, Lehigh Univ., Bethlehem, PA, May 1996.

[38]Liakopoulos, A., Blythe, P. A., and Gunes, H., "A Reduced Dynamical Model of Convective Flows in Tall Laterally Heated Cavities," *Proceedings of the Royal Society of London*, Vol. A453, No. 1958, 1997, pp. 663–672.

[39]Bonnet, J. P., Cole, D. R., Delville, J., Glauser, M. N., and Ukeiley, L. S., "Stochastic Estimation and Proper Orthogonal Decomposition: Complementary Techniques for Identifying Structure," *Experiments in Fluids*, Vol. 17, No. 5, 1994, pp. 307–314.

[40]Arndt, R. E., Long, D. F., and Glauser, M. N., "The Proper Orthogonal Decomposition of Pressure Fluctuations Surrounding a Turbulent Jet," *Journal of Fluid Mechanics*, Vol. 340, 1997, pp. 1–33.

[41]Gordeyev, S. V., and Thomas, F. O., "Coherent Structure in the Turbulent Planar Jet. Part 1. Extraction of Proper Orthogonal Decomposition Eigenmodes and Their Self-Similarity," *Journal of Fluid Mechanics*, Vol. 414, 2000, pp. 145–194.

[42]Freund, J. B., and Colonius, T., "POD Analysis of Sound Generation by a Turbulent Jet," AIAA Paper 2002-0072, Jan. 2002.

[43]Cipolla, K. M., Liakopoulos, A., and Rockwell, D., "Quantitative Imaging in Proper Orthogonal Decomposition of Flow past a Delta Wing," *AIAA Journal*, Vol. 36, No. 7, 1998, pp. 1247–1255.

[44]Sirovich, L., "Turbulence and Dynamics of Coherent Structures: I-III," *Quarterly of Applied Mathematics*, Vol. 45, No. 3, 1987, pp. 561–590.

[45]Liakopoulos, A., and Hsu, C. C., "On a Class of Compressible Laminar Boundary-Layer Flows and the Solution Behavior near Separation," *Journal of Fluid Mechanics*, Vol. 149, 1984, pp. 339–353.

A. Plotkin
Associate Editor